JACS
JOURNAL OF THE AMERICAN CHEMICAL SOCIETY
Article
pubs.acs.org/JACS

Calcium Inhibition of Ribonuclease H1 Two-Metal Ion Catalysis

Edina Rosta,*[,†,‡] Wei Yang,[§] and Gerhard Hummer*[,†,∥]

[†]Laboratory of Chemical Physics, National Institute of Diabetes and Digestive and Kidney Diseases, National Institutes of Health, Bethesda, Maryland 20892-0520, United States

[‡]Department of Chemistry, King's College London, London SE1 1DB, United Kingdom

[§]Laboratory of Molecular Biology, National Institute of Diabetes and Digestive and Kidney Diseases, National Institutes of Health, Bethesda, Maryland 20892, United States

[∥]Department of Theoretical Biophysics, Max Planck Institute of Biophysics, 60438 Frankfurt am Main, Germany

Supporting Information

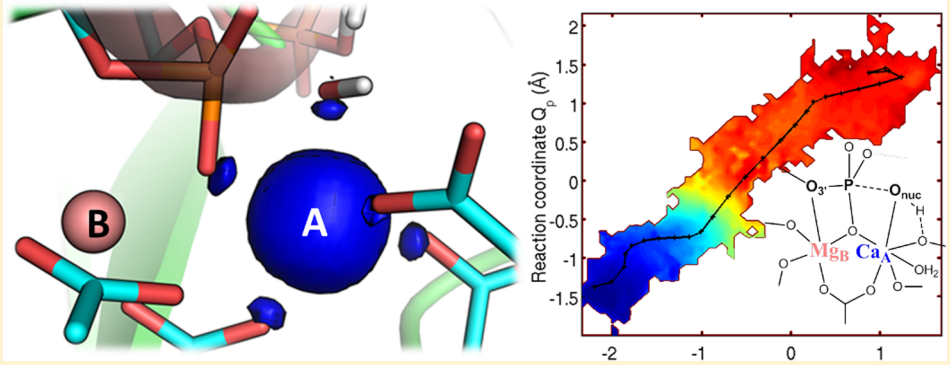

ABSTRACT: Most phosphate-processing enzymes require Mg^{2+} as a cofactor to catalyze nucleotide cleavage and transfer reactions. Ca^{2+} ions inhibit many of these enzymatic activities, despite Ca^{2+} and Mg^{2+} having comparable binding affinities and overall biological abundances. Here we study the molecular details of the calcium inhibition mechanism for phosphodiester cleavage, an essential reaction in the metabolism of nucleic acids and nucleotides, by comparing Ca^{2+}- and Mg^{2+} catalyzed reactions. We study the functional roles of the specific metal ion sites A and B in enabling the catalytic cleavage of an RNA/DNA hybrid substrate by *B. halodurans* ribonuclease (RNase) H1 using hybrid quantum-mechanics/molecular mechanics (QM/MM) free energy calculations. We find that Ca^{2+} substitution of either of the two active-site Mg^{2+} ions substantially increases the height of the reaction barrier and thereby abolishes the catalytic activity. Remarkably, Ca^{2+} at the A site is inactive also in Mg^{2+}-optimized active-site structures along the reaction path, whereas Mg^{2+} substitution recovers activity in Ca^{2+}-optimized structures. Geometric changes resulting from Ca^{2+} substitution at metal ion site A may thus be a secondary factor in the loss of catalytic activity. By contrast, at metal ion site B geometry plays a more important role, with only a partial recovery of activity after Mg^{2+} substitution in Ca^{2+}-optimized structures. Ca^{2+}-substitution also leads to a change in mechanism, with deprotonation of the water nucleophile requiring a closer approach to the scissile phosphate, which in turn increases the barrier. As a result, Ca^{2+} is less efficient in activating the water. As a likely cause for the different reactivities of Mg^{2+} and Ca^{2+} ions in site A, we identify differences in charge transfer to the ions and the associated decrease in the pK_a of the oxygen nucleophile attacking the phosphate group.

INTRODUCTION

The catalytic processing of nucleic acids and nucleotides is central in life, from the manipulation of genetic information to bioenergetics and signaling.[1−3] Many phosphoryl-transfer reactions rely on the ubiquitous two-metal ion catalysis (TMC) to form and break P−O bonds along the nucleic acid backbone and in polyphosphates. In TMC reactions, two divalent metal ions are positioned on opposite ends of the scissile phosphate bond, at the interface between the protein or ribozyme catalyst and the substrate. The metal ions facilitate an S_N2-type reaction, in which the nucleophilic "attacking" oxygen replaces the "leaving" oxygen in the broken P−O bond of the phosphate on the opposite side.[4,5] Similar Mg^{2+} ion selectivity has been found among many TMC enzymes; but in spite of numerous studies and detailed structural information,[6−9] the factors determining the functional competence[10−15] of different metal ions remain poorly understood.

Ca^{2+} and Mg^{2+} are the most abundant divalent metal ions in biological systems. Whereas Mg^{2+} is present inside the cell in millimolar concentrations (about ∼12 mM total [Mg^{2+}], and >0.5 mM free [Mg^{2+}]), Ca^{2+} is mainly found outside the

Received: November 8, 2013
Published: February 5, 2014

   dx.doi.org/10.1021/ja411408x | *J. Am. Chem. Soc.* 2014, 136, 3137−3144

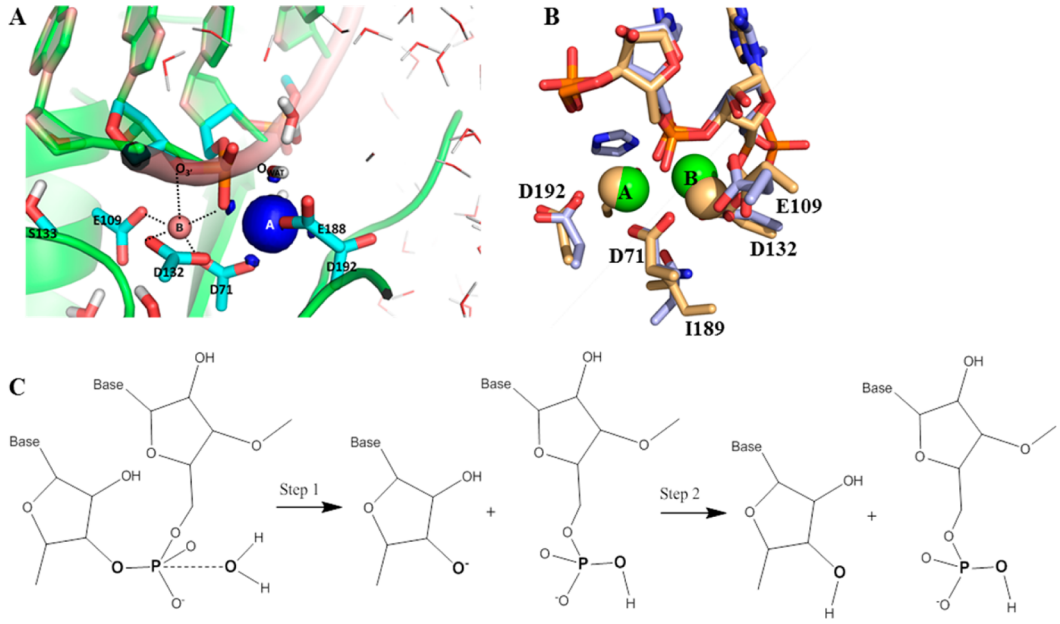

Figure 1. (A) Details of the quantum region in the RNase H1 active site of the MgMg system (protein and nucleic acid: cartoon representation; classical water molecules: lines; quantum region: atomic representation). The total electron density difference between the CaMg and MgMg systems is drawn at the 0.01 contour level (blue; au). Whereas the large blue sphere at the metal A site reflects the larger number of electrons on calcium, the small blue regions on the coordinated oxygen atoms illustrate the smaller extent of charge transfer from these ligands to Ca^{2+} as compared to Mg^{2+} (see also Figure S6 in Supporting Information [SI]). (B) Active site of RNase H1 in complex with two Ca^{2+} ions. Alignment between the minimized reactant-state structure (*B. halodurans,* orange carbon backbone and Mg^{2+} ions) and the crystallographic structure (*human*, PDB ID: 2QKK, blue carbon backbone and green Mg^{2+} ions) is shown for side chains and substrate within 4 Å of the Mg^{2+}. Water is omitted. (C) Schematics of the phosphodiester cleavage reaction catalyzed by RNase H1. In our calculations, we concentrate on the nucleophilic attack and phosphate−diester bond breaking (Step 1). Protonation of the ribose in Step 2 is not detailed here.[49]

cell.[16,17] Reflecting on the crucial role of Ca^{2+} in signaling processes, its concentrations are tightly regulated within intracellular compartments, typically in the nanomolar range.[17] An increase in the intracellular calcium concentration has been linked to apoptosis,[18] however it is not known whether the changes in the calcium concentration may also affect enzyme functions within cells to promote cell death. Interestingly, a number of enzymes using Mg^{2+} ions for catalysis are specifically inhibited by calcium despite their similar ionic properties. Examples of enzymes with calcium-inhibited catalytic activity for phosphate processing reactions include haloacid dehalogenases,[19,20] ATPases,[21−25] adenylyl cyclases,[26,27] kinases,[22,28,29] dUTPases,[30] polymerases,[31] and nucleases.[32−35] Interestingly, topoisomerases are able to catalyze the chemically identical phosphodiester cleavage reaction to nucleases in the presence of calcium, at an even faster rate than magnesium.[36] However, they are unable to carry out the religation of the cleaved DNA.[37] This results in a calcium-bound complex with cleaved DNA, similar to topoisomerase inhibitors.

To address the question of why calcium typically cannot catalyze phosphate cleavage and transfer, we study the prototypical Mg^{2+}-catalyzed phosphodiester cleavage in ribonuclease H1 (RNase H1) using hybrid quantum-mechanics/molecular mechanics (QM/MM) methods. The metal ions in TMC, labeled "A" and "B" (Figure 1A), likely play complementary roles in achieving the catalytic rate enhancement,[6] although the detailed mechanistic origins of these complementary roles are not fully elucidated. Importantly, in phosphodiester bond-cleavage reactions, metal ion A coordinates the oxygen atom carrying out the nucleophilic attack, whereas metal ion B interacts with the oxygen atom of the leaving group.[38,39] Experimentally, it is challenging, but not entirely impossible, to perform single metal substitutions to probe and separate the effects of the two ions. In particular, inactive mixed-metal ion structures have been determined crystallographically.[10,13] For ions with different binding affinities, variations in their concentrations could also be used to probe the effects of single metal substitutions on catalysis.[33−35] The relative affinities can also be modulated by mutations. Nonetheless, no clear consensus has emerged if sites A and B in TMC reactions are equally selective for metal ions, and if they are each inhibited by calcium.

Mg^{2+} is typically the required native cofactor for phosphate-catalyzing enzymes, whereas Ca^{2+} inhibits activity. These differences are primarily due to metal-specific changes in the catalytic rate (as shown for Ca^{2+}, for example, in the bacterial transposon Tn10[35] and in the yeast mitochondrial group II intron[40]), rather than due to changes in the product release rate (which can be rate limiting for other phosphoryl-transferases such as protein kinases[41]) or in the metal affinity. Metal binding appears to be relatively insensitive to the type of metal ion. Indeed, Ca^{2+} often has a higher binding affinity than Mg^{2+}, yet strongly inhibits catalysis in doubly substituted enzymes according to experiment[11,42−44] and quantum chemical calculations[45] on a variety of TMC systems. Mordasini et al.[45] found a large increase in the calculated energy barrier for doubly Ca^{2+}-substituted *Bam*HI endonuclease, which they attributed primarily to differences in the metal coordination geometries. However, it is not known if at least one of the two sites can tolerate an otherwise inhibitory Ca^{2+}.[33] Such single-site metal substitutions promise a more in-depth investigation of the different mechanistic roles of the two metal ions and of the overall reaction mechanism. Experimentally, biochemical

dx.doi.org/10.1021/ja411408x | *J. Am. Chem. Soc.* 2014, 136, 3137−3144

metal-ion rescue experiments may also be used to study single-ion sites using thiol-substituted enzymes.[13,46−48] These experiments can identify specific metal ion interactions by replacing a coordinating oxygen atom with sulfur, resulting in loss of activity with Mg^{2+}, and then subsequently regaining this activity upon the addition of Mn^{2+} or Cd^{2+}. However, to date, none of these experiments has succeeded in directly measuring the effects of single-metal ion replacements on TMC reaction rates.

Here we focus on the role of individual ions in the nucleic acid cleavage reaction (Figure 1C) catalyzed by ribonuclease H1. In RNase H1, two Mg^{2+} ions are the native cofactors catalyzing the nonspecific hydrolysis of the RNA strand of an RNA·DNA hybrid. The active site of RNase H1 is homologous to that of many other nucleic-acid processing enzymes, including the RNase H functionality of HIV reverse transcriptase.[50] High-resolution structures of RNase H1[51−54] (Figure 1A) have enabled detailed mechanistic studies[49,55−58] for this prototypical member of the TMC family.

In our calculations, we focus on TMC and do not address several factors that may affect the overall catalytic rate enhancement, in particular ion binding and changes in the solvation free energy.[59−61] A third metal site has been inferred from experiments, showing that addition of Ca^{2+} to enzyme−substrate solutions containing Mg^{2+} or Mn^{2+} activates catalysis,[33,34] and is documented in studies of several TMC systems, including alkaline phosphatase,[62,63] group I introns,[46,47,64] and DNA polymerase η.[65] However, the location of these metal ion sites may vary in different systems. We also do not consider three metal-ion catalytic mechanisms, as used by other enzymes cleaving phosphodiester bonds, such as the DNA repair enzyme endonuclease IV.[66,67] In the structure of RNase H1, no third metal ion was found at concentrations of $MgCl_2$ as high as 300 mM.[54]

We use high-dimensional string quantum-mechanics/molecular mechanics (QM/MM) free energy calculations in conjunction with novel enhanced-sampling techniques to probe the functional roles of specific metal ion sites in enabling TMC in RNase H1. Such calculations allow us to map the detailed free energy profiles and mechanism of enzymatic reactions.[68] We develop a new string[69] free energy simulation method coupled with Hamiltonian replica exchange to study the first step of the RNA hydrolysis reaction catalyzed by RNase H1. To optimize the sampling efficiency, we space the string images in a nonequidistant manner, aiming for an image density proportional to the free energy gradient along the reaction profile. These extensive QM/MM free energy calculations employing a 20-dimensional reaction coordinate provide us with a full thermal sampling of the entire reaction pathway. The free energy profiles calculated for calcium-bound enzymes show that even a single-ion Ca^{2+} substitution of Mg^{2+} can abolish catalytic activity.

METHODS

The QM/MM calculations were initiated from the X-ray crystal structure of the *B. halodurans* RNase H1 enzyme complexed with a hybrid RNA.DNA duplex substrate, and with both metal sites occupied by Mg^{2+} (PDB code 1ZBI[51]). The complex was solvated by adding water and ions, and prepared for simulations as described earlier.[49] The quantum region included 91 atoms. The equilibrated classical region surrounding the quantum region was trimmed to a sphere of 20 Å radius centered on the middle of the distance between the two Mg^{2+} metal ions, and neutralized by removing excess chloride ions.

We focused on the rate-limiting first step of the catalytic reaction in which a water molecule associated with metal ion A is deprotonated and attacks the phosphate group. This nucleophilic attack results in the cleavage of the distal P−O bond, and in the release of an unprotonated ribose that coordinates metal ion B.[49] In a second step, involving a lower barrier and a strong energetic driving force, the ribose leaving group is protonated and released from ion B.[49] By leaving the proton donor Asp132 unprotonated,[49] we stalled the reaction after the first step. We note that in an earlier calculation of the MgMg system,[57] we had used a smaller quantum region that did not include the downstream phosphate accepting the proton in the initial reaction step. As a result, the proton abstracted from the nucleophilic water was instead transferred to the scissile phosphate, resulting in a significantly higher free energy barrier of ∼21 kcal/mol[57] compared to the ∼17 kcal/mol[49] with the larger quantum region used also here.

Q-Chem[70] was used for the QM calculations at the B3LYP[71] 6-31+G(d) level of density functional theory. QM and MM systems were coupled in the CHARMM program[72,73] using full electrostatic embedding[74] and standard link atom treatment, adding hydrogen atoms for the missing ligands. Langevin dynamics was run at a temperature of 300 K with a 1 fs time step.

To determine the free energy surface underlying the reactions in the CaMg and MgCa systems, we performed string[69] simulations, in which we extended our earlier implementation[49] to higher dimensions. The string representing the reaction pathway was calculated in a 20-dimensional space of atom−atom distances, as listed in Figure S2 and Table S1 in SI. To accelerate equilibration and sampling, we ran the umbrella sampling simulations for the different windows in parallel and coupled them with Hamiltonian replica exchange,[75] attempting exchanges of the structures between neighboring windows at exchange intervals of 20 fs.

We used a nonlinear optimization procedure to update the positions of the 26 structures (or "images") representing the string with an image density approximately proportional to the free energy gradient along the reaction profile. We developed an improved method to place the images along the string and to determine the force constants of the harmonic bias for each image in each dimension. The spring constants K of the restraining potentials are assigned on the basis of the mean force acting at the center of the restraint along the reaction coordinates. Intuitively, more rigid restraints are needed in regions with steep free energy gradients. Accordingly, we assigned the force constants in the iteration k, for the ith dimension and jth image as:

$$K_{ij}^{k} = \max\left(\min\left(K_{\max}, \frac{\Delta_{ij}^{k-1}}{\delta_i} K_{ij}^{k-1}\right), K_{\min}\right)$$

where $\Delta_{ij}^{k-1} = |c_{ij}^{k-1} - \overline{q}_{ij}^{k-1}|$ is the absolute value of the mean deviation of the reaction coordinate q_i from its constraint center c_{ij}^{k-1} in the iteration $k-1$, for the jth image. The average value of the coordinate is denoted by $\overline{q}_{ij}^{k-1}$ The threshold parameter δ_i of 0.05 Å was constant for all reaction coordinates, $K_{\min}$ was 1 kcal mol^{-1} Å^{-2}, and $K_{\max}$ was 150 kcal mol^{-1} Å^{-2}. The force constant determination was thus designed to provide an average deviation from the constraint positions approximately equal to the threshold value δ_i along each dimension in the string for all images.

After each iteration, the images were redistributed along the string according to a new update scheme. We aimed to determine the positions in the next iteration step such that the average acceptance probability for switching the configurations between the neighboring images by Hamiltonian replica exchange is approximately equal along the string. Assuming δ_i is negligible compared with $|c_{ij}^{k} - c_{ij+1}^{k}|$, the average acceptance probability, $p_{j\leftrightarrow j+1}^{k}$, between images j and $j+1$ for iteration k can be approximated in the following form:

$$p_{j\leftrightarrow j+1}^{k} \approx \exp\left(-\beta \sum_{i=1}^{M} \frac{K_{ij}^{k} + K_{ij+1}^{k}}{2} (c_{ij}^{k} - c_{ij+1}^{k})^2\right)$$

with M being the number of reaction coordinates used to describe the string, and $\beta = 1/k_B T$ the inverse temperature. We defined the first and last images such that their constraint positions correspond to the respective average positions obtained from the k-th iteration: $c_{i1}^{k+1} \equiv \overline{q}_{i1}^{k}$

dx.doi.org/10.1021/ja411408x | J. Am. Chem. Soc. 2014, 136, 3137−3144

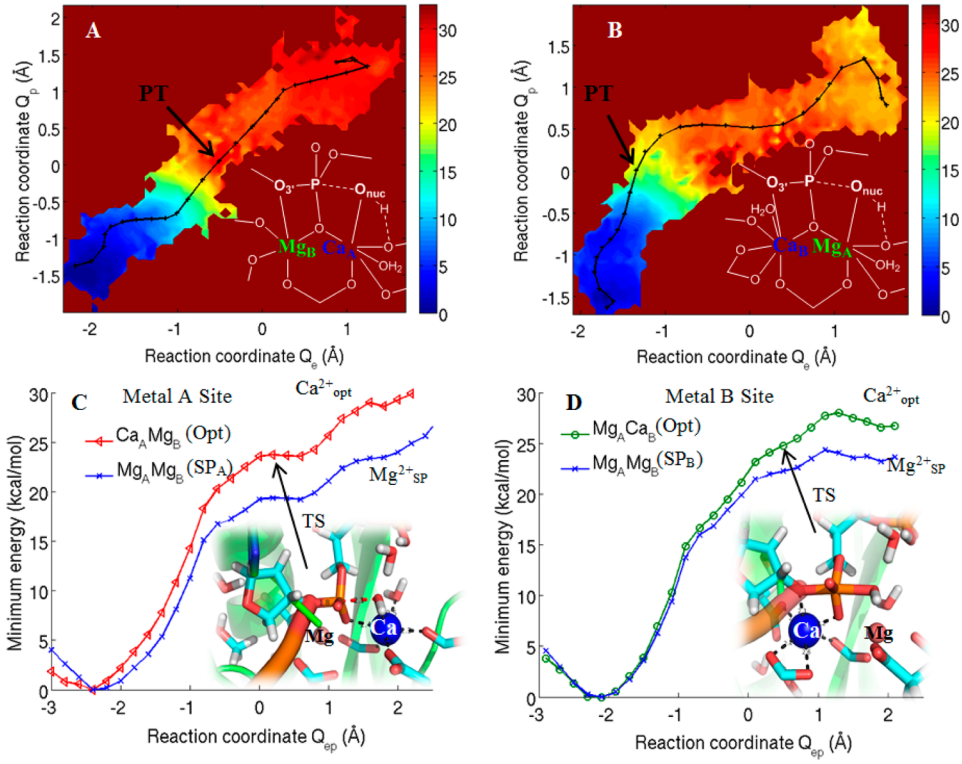

Figure 2. Reaction free energy and minimum energy profiles for single Ca^{2+} substitutions in RNase H1: (A) 2D free energy surface of the CaMg system projected on Q_e-Q_p plane (scale bar in kcal/mol). Q_e is defined as the difference between the bond-breaking and bond-forming P−O distances, Q_p is the proton transfer coordinate defined as the difference between the bond-breaking and bond-forming O−H distances (see also Figure S2 in SI). The converged string is shown in black. (B) 2D free energy surface of the MgCa system. The converged string is shown in black. Insets in A and B indicate the metal coordination geometry. (C) Energy minimized pathway for the CaMg system (red, triangles, labeled "Opt"). Q_{ep} is defined as the sum of Q_e and Q_p (Figure S2 in SI). Single-point QM/MM energies at the same level of theory are also shown for MgMg (blue, crosses, labeled "SP") obtained by substituting Mg^{2+} for Ca^{2+} in energy minimized CaMg structures along the reaction pathway without further relaxation. (D) Energy minimized pathway for the MgCa system (green circles, labeled "Opt"). In (C) and (D), single-point QM/MM energies at the same level of theory are also shown for MgMg (blue, crosses, labeled "SP") obtained by replacing Ca^{2+} with Mg^{2+} using the coordinates obtained from the CaMg energy minimized pathway, without further relaxation. Insets in C and D show TS structures, as indicated by the arrows.

and $c_{iN}^{k+1} \equiv \bar{q}_{iN}^{k}$. Assuming that the force constants remain unchanged from the k-th iteration, we determined the values for c_{ij}^{k+1}, $j = 2,..., N-1$, such that $p_{j\leftrightarrow j+1}^{k+1}$ is constant for all $j = 1,...,N-1$. This image-redistribution scheme together with the force constant assignment results in an image density that is approximately proportional to the square-root of the gradient of the free energy along the string.

We measured the string convergence by calculating the RMSD between the final constraint positions and the mean positions from the 10 previous iterations:

$$\max_{i=1,...,M} \sqrt{\frac{1}{N}\sum_{j=1}^{N}\left(c_{ij}^{k+1} - \frac{\sum_{l=k-10}^{k} c_{ij}^{l}}{10}\right)^2}$$

The maximum RMSD values along all dimensions were below 0.15 Å in both sets of free energy simulations. The total times used for analysis were 118 and 125 ps for MgCa and CaMg, respectively, including all 26 images along the string. The data from the string simulations described below were unbiased using a histogram-free version of the "multidimensional weighted histogram analysis method" (WHAM).[76]

RESULTS AND DISCUSSION

Ca^{2+} Substitutions Abolish the Catalytic Activity. We calculated the free energy surfaces corresponding to the catalytic reactions with single Ca^{2+} ions substituting the native Mg^{2+} at sites A (CaMg) and B (MgCa). The starting molecular models of the Ca-substituted systems were generated on the basis of structures from our previous QM/MM study.[49] Following the substitution of metal ions at site A or B, we carried out additional energy minimizations, as well as QM/MM dynamics to determine the free energy surfaces underlying the catalytic reaction. As a result of the substitutions, the free energy barrier for the first (and dominant) reaction step increased from ∼17 kcal/mol in the enzyme with the two native Mg^{2+} ions bound (MgMg[49] with Asp132 unprotonated; see Figure S2 in ref 49) to ∼25 kcal/mol (CaMg) and ∼24 kcal/mol (MgCa) (Figures 2 and S3 in SI). In this first reaction step, an OH^- nucleophile is formed by proton transfer from the attacking water molecule to the downstream phosphate. This nucleophile attacks the phosphate group and breaks the sugar−phosphate bond of the RNA strand (Figure 1C). The ribose leaving group is coordinated to metal B, and becomes protonated only later, in the second step.[49]

To test the free energy profiles of the first step, we also performed energy minimizations starting from the thermally equilibrated structures of the string simulations. We find that the energetics and reaction pathways obtained from energy minimizations are consistent with the free energy calculations, both for the native metal cofactors and for the Ca^{2+}-substituted systems (SI text sections III−IV and C and D of Figure 2 and Figure S3 in SI). In the energy profiles in Figures 2 C and D, and S4 in SI as reference, the energy barriers at Q_{ep}∼0.5 Å are ∼19 kcal/mol (MgMg), ∼24 kcal/mol (CaMg), and ∼25 kcal/

dx.doi.org/10.1021/ja411408x | J. Am. Chem. Soc. 2014, 136, 3137−3144

mol (MgCa), all within 2 kcal/mol of the calculated free energy barriers. The minimum free energy path is thus close to a minimum energy path, as would be expected for a chemical reaction involving significant motions only along a limited number of degrees of freedom.[77] Accordingly, we performed energy minimizations also on the enzyme in which both metal ion binding sites are occupied by Ca^{2+}, and no Mg^{2+} is present (CaCa system). The high energy barrier of ∼29 kcal/mol (Figure S5 in SI) estimated from these minimizations is consistent with the experimentally observed inhibition, and with the cumulative effects of the single ion substitutions at metal sites A and B.

Interestingly, Ca^{2+} substitution at the A site also changes the mechanistic character of the reaction. For the MgMg and MgCa systems, the saddle in the 2D free energy surface of the first step of the RNase H1 reaction is oriented entirely along the proton transfer direction Q_p, without significant dependence on the P−O bond forming and breaking coordinate Q_e (bent, Γ-shaped reaction pathway in Figure S2 of ref 49 and Figure 2B, respectively). With Mg^{2+} at the A site, motion through the TS is thus dominated by the proton transfer away from the activated water and toward the downstream phosphate accepting it. By contrast, in a 2D Q_e−Q_p projection of the CaMg reaction free energy surface, the saddle is oriented diagonally instead of horizontally (nearly straight pathway in Figure 2A). In CaMg, passage through the transition state thus involves strongly coupled motions of the proton away from the activated water to the downstream phosphate, and of the forming and breaking P−O bonds. The 2D free energy surfaces also indicate that with Ca^{2+} at the metal A site, the barrier is located at a larger value of $Q_p \approx 1$ Å, as compared to ∼0.5 Å for Mg^{2+}. This shift of the TS toward larger Q_p indicates that, as one factor for the higher barrier, Ca^{2+} is less effective in activating the nucleophilic water than Mg^{2+}.

Geometrical Changes upon Ca^{2+} Substitution. Substitution of Mg^{2+} by Ca^{2+} induced local structural changes. In particular, the metal−ligand distances increased from ∼2.1 Å to ∼2.4 Å on average both in the string simulations and in minimized structures (Table S2 in SI). In addition, the metal−metal distances increased by about 0.1 Å (Table S2 in SI). These changes are in agreement with previous studies,[53,78] and also an independently determined CaCa X-ray structure of human RNase H1[53] (PDB ID: 2QKK). As shown in Figure 1B, a structural alignment shows excellent agreement between our minimized CaCa structure and the X-ray structure 2QKK. A small shift in the Ca^{2+} B position between 2QKK and our structure is likely caused by the D210N mutation in the human enzyme corresponding to the D132 residue in *B. halodurans*, which coordinates metal ion B. Also note that E188 is replaced by a histidine residue (H264) in the human enzyme. Importantly, in the experimental structure the metal ion coordination is unchanged in the CaCa enzyme, except for the longer bond lengths with Ca^{2+}, both being correctly reproduced in our calculations.

To quantify the effects of the Ca^{2+}-induced changes in the structure, we used single-point energy calculations with Mg^{2+} put into Ca^{2+}-optimized structures, and vice versa. In this way, we can separate the effects of the longer ligand bond distances with Ca^{2+}, and of the changed metal ion coordination geometry, from nonstructural effects. Specifically, we used the minimized structures along the reaction pathway obtained for the MgMg system, substituted Mg^{2+} with Ca^{2+}, and recalculated the QM/MM energies without further relaxation (Table S2 and Figure S4 in SI).

Remarkably, our calculations largely rule out geometric relaxations at the metal ion A site as a major factor[79] for the Ca^{2+}-induced loss in catalytic activity. Without changes in the metal-ion coordination geometry, due to the Ca^{2+} substitution, the energy barrier is ∼8 kcal mol^{-1} higher in the CaMg system than in the MgMg system for metal ion A replacement, consistent with the difference in the free energy barriers obtained for the fully relaxed structures. Conversely, when we used the fully relaxed CaMg structures, and replaced the Ca^{2+} ion by Mg^{2+} without further relaxation, the energy barrier decreased to about the value of the MgMg system (Figure 2C). In both profiles a shoulder appears (near $Q_{rp} = 0$); the corresponding transition state (TS) structure for CaMg is shown in the inset. This shoulder corresponds to (i) the deprotonation of the nucleophilic water, and (ii) to an approach of the OH^- group to a distance of about 2.1 Å from the phosphorus atom. At this phase of the reaction (Figure 2C), the energy difference between the MgMg and CaMg systems is largest. During the subsequent part of the reaction, when the chemical bond breaking and forming occurs, the energy profiles remain close to parallel; note that the product energies remain high because only the first and rate-determining step was probed.[49] This suggests that the main reason for the difference in the energy barriers between the MgMg and CaMg systems is the increased energy cost of the deprotonation of the Ca^{2+}-bound water. With Mg^{2+} being active even in a Ca^{2+}-optimized coordination geometry, and with Ca^{2+} being inactive irrespective of geometry, we rule out geometry changes as a main cause for the loss of catalytic activity at site A in the Ca^{2+}-substituted enzyme.

Note that the MgMg energy profiles obtained by Mg^{2+} substitutions into Ca^{2+}-optimized structures (blue curves in C and D of Figure 2) are not identical to the energy profile obtained for the MgMg system (Figure S4 in SI), or to each other, because each one is based on different underlying structures and pathways. In Figure 2C, the pathway and geometries correspond to the CaMg optimized pathway, whereas in Figure 2D, the pathway and geometries correspond to the MgCa optimized pathway. Both of these are different from the MgMg optimized pathway (Figure S4 in SI), with the main geometrical differences arising from the changes in the metal−ligand coordination around the Ca^{2+} ions.

We found earlier that at the metal ion site B the coordination geometry becomes more symmetrical as the transition state is approached along the reaction profile.[49] Thus, geometrical changes at site B[49] likely contribute more to the inactivity of the MgCa system. Indeed, unlike for CaMg we do not fully recover activity when Mg^{2+} is substituted back into the structures along the pathway optimized for MgCa (compare MgMg curves in Figures 2D and Figure S4 in SI). Similarly, when Ca^{2+} is substituted back into the optimized MgMg structures along the reaction pathway without reoptimization of the geometries, the energy barrier only slightly increases (green curve in Figure S4 in SI) compared to fully geometry optimized MgCa (green curve in Figure 2D). The geometry determined with the Mg^{2+} ion at the B position thus supports catalysis even with Ca^{2+} substituted, but activity for the phosphate cleavage step of the reaction (Step 1, Figure 1C) is lost when the structure relaxes to accommodate a Ca^{2+} ion at the B site. Interestingly, there are several changes in the metal ion B coordination geometry during the first reaction step of the RNA backbone cleavage. To

dx.doi.org/10.1021/ja411408x | J. Am. Chem. Soc. 2014, 136, 3137−3144

quantify these changes, we calculated the Mg_B and Ca_B coordination distances with the oxygen atoms of nearby groups from the last 1.1 ps of our string simulations in CaMg and MgCa, respectively (Figures S8 and S9 in SI). Interestingly, the Ca^{2+} ion bound at site B is also coordinated by a water molecule throughout most of the profile, and Mg^{2+} also coordinates the equivalent water molecule in the reactant state (Figures S8 and S9 in SI). This water molecule (WAT 26 in the 1ZBL structure) is present in most high-resolution structures (e.g., PDB ID: 1ZBL, 1ZBI, 2G8F, or 2QKK). In CaMg, the Mg^{2+} in the metal ion B position initially has six coordination ligands: D71, D132 (with bidentate coordination), E109, WAT 26, and the RNA O2P with a slightly longer coordination distance. Subsequently, WAT 26 leaves the coordination sphere of the Mg^{2+} ion, whereas the RNA O2P moves closer. At the TS, the RNA O3′ leaving group also moves closer, to eventually coordinate the Mg^{2+}, while the coordination of D132 changes from bidentate to monodentate. In MgCa, the Ca^{2+} in the metal ion B position has more coordination ligands, WAT 26 remains coordinated along most of the reaction profile. Similar to CaMg, the RNA O2P moves closer as the TS is approached, and then further away in the product state of step one. The RNA sugar O3′ moves closer such that the metal ion can stabilize the building negative charge on the leaving group. As a striking difference between the two metal ions, the Ca^{2+} coordination geometry exhibits much larger flexibility than that of the rigid Mg^{2+} ion. This can be seen by the much larger fluctuations of the Ca^{2+} coordination distances than Mg^{2+}, despite the fact that the force constants of the harmonic restraint potentials in the string simulations were largely similar. The conserved water molecule, the more restricted coordination geometry of Mg^{2+}, and the interconversion between penta- and hexa-coordinated structures,[54] are all likely to factor into the catalytic efficiency of the enzyme.[49]

Different Charge Transfer Efficiency of Ca^{2+} vs Mg^{2+}. Searching for possible physicochemical factors[80] that determine metal activity at the A site, we observed significant differences in the transfer of partial charge from the ligands to the metal ions (Table S3 in SI). In the MgMg system, the effective charge of ion A was reduced from its nominal value of 2 *e* to ∼1.9 *e* in the reactant state (RS), and it decreased even further to ∼1.8 *e* in the transition state (TS, see Methods). By contrast, in the CaMg system, Ca^{2+} retained its nominal charge, with effective values of ∼2.0 and ∼1.9 *e* in the RS and TS, respectively. Figures 1A and S6 in SI show the increased electron density on the Ca^{2+} ligand atoms at the transition state, including the nucleophilic water. Corresponding differences in charge transfer efficiency have also been observed in quantum chemical calculations of ion−water clusters, where the Mulliken partial charges of Mg^{2+} were consistently smaller than those of Ca^{2+}.[78]

Charge transfer to metal ion A at the TS likely helps activate the nucleophilic water molecule, providing a possible contributing factor for the change in reactivity between Mg^{2+} and Ca^{2+}. An earlier calculation[56] by De Vivo et al. showed that substituting the water nucleophile by hydroxide lowered the reaction barrier by ∼5.5 kcal/mol, supporting our conclusion that water deprotonation is a substantial contributor to the overall barrier. Note that the difference between the effective pK_a of the hydrated Mg^{2+} and Ca^{2+} ions in bulk water is less than 2,[81] which would not account for the observed difference in the energy barriers from our calculations. By contrast, the calculated pK_a of a single water molecule bound to the metal ion in the gas phase is significantly lower for Mg^{2+} than for Ca^{2+} (14.1 kcal/mol in Table S4 in SI, corresponding to a pK_a difference of ∼10). The difference between solution and gas phase is likely due to a combination of dielectric solvation effects and differences in the metal coordination geometry of the two ions. Since in the enzyme active site the preorganized charged groups provide a relatively rigid environment, we expect the pK_a difference of the water nucleophile bound to Mg^{2+} and to Ca^{2+} to be intermediate between solution and gas phase values.

The important role of activating the nucleophilic water is also reflected in the change of mechanism reported above for the CaMg system. With Ca^{2+} at the A site, less charge is transferred from the water ligand to the ion, such that the water ligand does not as readily give up its proton. As shown in Figure 3,

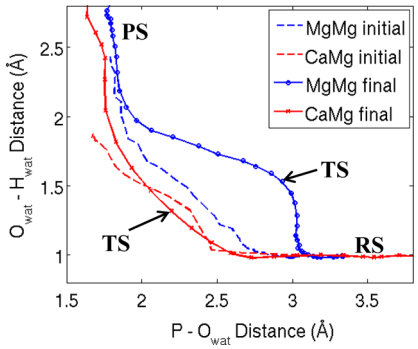

Figure 3. Reaction pathways projected onto the distances of the oxygen atom of the nucleophilic water to the scissile phosphate (P−O, *x*-axis) and to the proton abstracted from the nucleophile (O−H, *y*-axis). The average distances of the last iteration in the string free energy simulations are shown for MgMg (blue) and CaMg (red). The initial pathways, before the string iterations, are shown as dashed lines. Product state (PS), transition state (TS), and reactant state (RS) distances are indicated.

with Ca^{2+} at the metal A site, deprotonation of the water nucleophile occurs at a much closer P−O distance of ∼2.7 Å to the scissile phosphate compared to the ∼3 Å distance in the presence of Mg^{2+}. Moreover, nucleophile deprotonation and P−O bond formation in the presence of Ca^{2+} at the A site are highly concerted, with P−O and O−H bond lengths changing in unison. The proton is gradually forced off the water as one P−O bond breaks and the other one forms, resulting in the higher barrier and a TS at larger Q_p discussed above. By contrast, with Mg^{2+}, the two reaction steps have a more sequential character according to the MgMg pathway in Figure 3. Overall, these mechanistic differences are consistent with Ca^{2+} being less efficient in activating water than Mg^{2+}, with a reduced charge transfer from the nucleophile to the Ca^{2+} ion being a likely underlying factor.

■ CONCLUSIONS

This study is aimed at elucidating the role of individual ions in the nucleic acid cleavage reaction (Figure 1C) catalyzed by ribonuclease H1 (RNase H1). It is also motivated by the question, How does Ca^{2+} inhibit catalysis in phosphate processing reactions, despite its similarity to Mg^{2+} with respect to both binding affinity and active-site structure.

We used QM/MM simulations to study the mechanistic details of TMC in RNase H1, which serves as a prototypical member of a superfamily of enzymes involved in the processing

of nucleic acids and polyphosphates.[82,83] To examine complementary roles of the two metal ions A and B in TMC enzymes, we probed the effect of single ion substitutions in RNase H1 by using high-dimensional string QM/MM free energy simulations. Our calculations demonstrate that single ion substitutions at either metal site A or B from Mg^{2+} to Ca^{2+} abolish catalysis in the RNase H1 catalytic reaction. The increase in barrier height of ∼8 kcal/mol upon calcium substitution is consistent with the absence of RNA cleavage on a time scale of hours for *E. coli* RNase H1.[84]

Whereas the active-site architecture is largely unaffected, changes in ion coordination geometry are found upon Ca^{2+} substitution, due primarily to increases in ligand−metal bond distances. Remarkably, these changes affect the activity differently at metal ion sites A and B. By separating geometry effects from chemical effects resulting from the metal-ion substitutions, we could show that geometric changes play a significant role in controlling activity at metal ion site B. By contrast, metal ion A is less sensitive to its local coordination geometry, and the different extent of metal−ligand charge transfer may be responsible for the decreased activity with Ca^{2+} as compared to Mg^{2+}.

Remarkably, ribozymes also use TMC with active-site architectures similar to that of RNase H1,[3] for example, RNase P.[85,86] Catalytic rates for *E. coli* RNase P with Mg^{2+} and Ca^{2+} were reported to differ by a factor of ∼15,000,[87] corresponding to a barrier increase of ∼6 kcal/mol. Allowing for differences in the active site and reaction mechanism,[86] and taking into account the difficulties to fully remove Mg^{2+} ions from ribozymes, this increase is in a reasonable agreement with our calculated value for RNase H1. Group I and group II introns have also been found to be inactive with Ca^{2+}.[88−90] Our simulation results, combined with structural studies, might shed light on how Ca^{2+}-active variants of the otherwise Ca^{2+}-inactive Tetrahymena group I intron[88,89] could be found by in vitro evolution.[91]

We also note that at high concentrations of metal ions, a possible third metal-ion binding site[55] could become populated in RNase H1. This third site helps rationalize experiments[92] showing attenuation effects at high Mg^{2+} concentration. A potential third metal-ion binding site could also modulate the activity of systems with mixed-metal-ion solutions.[46,55,62,63,93] Since here we did not explore the effects of a third metal ion directly, we cannot comment directly on an activating role of Ca^{2+} at a third metal-binding site at low Ca^{2+} concentrations. However, our calculations clearly show that at higher concentrations, Ca^{2+} would be inhibitory due to the Ca^{2+} binding at the A or B sites. With hydrolysis being a central step in TMC, the mechanistic principles found here for *B. halodurans* RNase H1 likely apply broadly to other TMC systems.

■ ASSOCIATED CONTENT

Supporting Information

Methods, active site and reaction coordinates, free energy of Ca substituted systems, energy minimizations, metal ion coordination geometry, charge transfer and gas phase acidity, full author list for refs 70 and 73. This material is available free of charge via the Internet at http://pubs.acs.org.

■ AUTHOR INFORMATION

Corresponding Authors

Edina.Rosta@kcl.ac.uk (E.R.)

Gerhard.Hummer@biophys.mpg.de (G.H.)

Notes

The authors declare no competing financial interest.

■ ACKNOWLEDGMENTS

We thank Drs. Bernard Brooks, Yihan Shao, and Nicolae-Viorel Buchete for their valuable help. This work was supported by the Intramural Research Program of the National Institute of Diabetes and Digestive and Kidney Diseases, National Institutes of Health, and by the Max Planck Society (G.H.), and used the computational resources of the NIH Biowulf Cluster (http://biowulf.nih.gov).

■ REFERENCES

(1) Stahley, M. R.; Strobel, S. A. *Science* **2005**, *309*, 1587.
(2) Sträter, N.; Lipscomb, W. N.; Klabunde, T.; Krebs, B. *Angew. Chem., Int. Ed.* **1996**, *35*, 2024.
(3) Yang, W.; Lee, J. Y.; Nowotny, M. *Mol. Cell* **2006**, *22*, 5.
(4) Beese, L. S.; Steitz, T. A. *EMBO J.* **1991**, *10*, 25.
(5) Gerlt, J. A.; Coderre, J. A.; Mehdi, S. *Adv. Enzymol. Relat. Areas Mol. Biol.* **1983**, *55*, 291.
(6) Yang, W. *Nat. Struct. Mol. Biol.* **2008**, *15*, 1228.
(7) Yang, W. *Q. Rev. Biophys.* **2011**, *44*, 1.
(8) Cisneros, G. A.; Perera, L.; Schaaper, R. M.; Pedersen, L. C.; London, R. E.; Pedersen, L. G.; Darden, T. A. *J. Am. Chem. Soc.* **2009**, *131*, 1550.
(9) Fothergill, M.; Goodman, M. F.; Petruska, J.; Warshel, A. *J. Am. Chem. Soc.* **1995**, *117*, 11619.
(10) Brautigam, C. A.; Steitz, T. A. *J. Mol. Biol.* **1998**, *277*, 363.
(11) Bellamy, S. R. W.; Kovacheva, Y. S.; Zulkipli, I. H.; Halford, S. E. *Nucleic Acids Res.* **2009**, *37*, 5443.
(12) Perona, J. J. *Methods* **2002**, *28*, 353.
(13) Brautigam, C. A.; Sun, S.; Piccirilli, J. A.; Steitz, T. A. *Biochemistry* **1999**, *38*, 696.
(14) Bowman, J. C.; Lenz, T. K.; Hud, N. V.; Williams, L. D. *Curr. Opin. Struct. Biol.* **2012**, *22*, 262.
(15) Zheng, X. H.; Mueller, G. A.; DeRose, E. F.; London, R. E. *Nucleic Acids Res.* **2012**, *40*, 10543.
(16) Rink, T. J.; Tsien, R. Y.; Pozzan, T. *J. Cell Biol.* **1982**, *95*, 189.
(17) Carafoli, E. *Nat. Rev. Mol. Cell Biol.* **2003**, *4*, 326.
(18) Orrenius, S.; Zhivotovsky, B.; Nicotera, P. *Nat. Rev. Mol. Cell. Biol.* **2003**, *4*, 552.
(19) Neuhaus, F. C.; Byrne, W. L. *J. Biol. Chem.* **1959**, *234*, 113.
(20) Peeraer, Y.; Rabijns, A.; Collet, J. F.; Van Schaftingen, E.; De Ranter, C. *Eur. J. Biochem.* **2004**, *271*, 3421.
(21) Beauge, L.; Campos, M. A. *Biochim. Biophys. Acta. - Biomembr.* **1983**, *729*, 137.
(22) Skou, J. C. *Biochim. Biophys. Acta* **1957**, *23*, 394.
(23) Fukushima, Y.; Post, R. L. *J. Biol. Chem.* **1978**, *253*, 6853.
(24) Knauf, P. A.; Proverbio, F.; Hoffman, J. F. *J. Gen. Physiol.* **1974**, *63*, 324.
(25) Collins, K.; Sellers, J. R.; Matsudaira, P. *J. Cell Biol.* **1990**, *110*, 1137.
(26) Colvin, R. A.; Oibo, J. A.; Allen, R. A. *Cell Calcium* **1991**, *12*, 19.
(27) Oldham, S. B.; Rude, R. K.; Molloy, C. T.; Lipson, L. G.; Boggs, T. T. *Endocrinology* **1984**, *115*, 1883.
(28) Ryves, W. J.; Dajani, R.; Pearl, L.; Harwood, A. J. *Biochem. Biophys. Res. Commun.* **2002**, *290*, 967.
(29) Lu, S.-Y.; Huang, Z.-M.; Huang, W.-K.; Liu, X.-Y.; Chen, Y.-Y.; Shi, T.; Zhang, J. *Proteins: Struct., Funct., Bioinf.* **2013**, *81*, 740.
(30) Mol, C. D.; Harris, J. M.; McIntosh, E. M.; Tainer, J. A. *Structure* **1996**, *4*, 1077.
(31) Irimia, A.; Zang, H.; Loukachevitch, L. V.; Eoff, R. L.; Guengerich, F. P.; Egli, M. *Biochemistry* **2006**, *45*, 5949.
(32) Bennett, S. P.; Halford, S. E. *Curr. Top. Cell. Regul.* **1989**, *30*, 57.

(33) Pingoud, V.; Wende, W.; Friedhoff, P.; Reuter, M.; Alves, J.; Jeltsch, A.; Mones, L.; Fuxreiter, M.; Pingoud, A. *J. Mol. Biol.* **2009**, *393*, 140.
(34) Vipond, I. B.; Baldwin, G. S.; Halford, S. E. *Biochemistry* **1995**, *34*, 697.
(35) Junop, M. S.; Haniford, D. B. *EMBO J.* **1996**, *15*, 2547.
(36) Deweese, J. E.; Osheroff, N. *Metallomics* **2010**, *2*, 450.
(37) Osheroff, N.; Zechiedrich, E. L. *Biochemistry* **1987**, *26*, 4303.
(38) Horton, N. C.; Perona, J. J. *Nat. Struct. Mol. Biol.* **2001**, *8*, 290.
(39) Steitz, T. A.; Steitz, J. A. *Proc. Natl. Acad. Sci. U.S.A.* **1993**, *90*, 6498.
(40) Erat, M. C.; Sigel, R. K. O. *J Biol Inorg Chem* **2008**, *13*, 1025.
(41) Jacobsen, D. M.; Bao, Z.-Q.; O'Brien, P.; Brooks, C. L.; Young, M. A. *J. Am. Chem. Soc.* **2012**, *134*, 15357.
(42) Newman, M.; Lunnen, K.; Wilson, G.; Greci, J.; Schildkraut, I.; Phillips, S. E. V. *EMBO J.* **1998**, *17*, 5466.
(43) Casareno, R. L. B.; Cowan, J. A. *Chem. Commun.* **1996**, 1813.
(44) Babu, C. S.; Dudev, T.; Casareno, R.; Cowan, J. A.; Lim, C. *J. Am. Chem. Soc.* **2003**, *125*, 9318.
(45) Mordasini, T.; Curioni, A.; Andreoni, W. *J. Biol. Chem.* **2003**, *278*, 4381.
(46) Hougland, J. L.; Kravchuk, A. V.; Herschlag, D.; Piccirilli, J. A. *PLoS Biol.* **2005**, *3*, e277.
(47) Forconi, M.; Lee, J.; Lee, J. K.; Piccirilli, J. A.; Herschlag, D. *Biochemistry* **2008**, *47*, 6883.
(48) Cohn, M.; Shih, N.; Nick, J. *J. Biol. Chem.* **1982**, *257*, 7646.
(49) Rosta, E.; Nowotny, M.; Yang, W.; Hummer, G. *J. Am. Chem. Soc.* **2011**, *133*, 8934.
(50) Le Grice, S. F. J. *J. Biol. Chem.* **2012**, *287*, 40850.
(51) Nowotny, M.; Gaidamakov, S. A.; Crouch, R. J.; Yang, W. *Cell* **2005**, *121*, 1005.
(52) Nowotny, M.; Cerritelli, S. M.; Ghirlando, R.; Gaidamakov, S. A.; Crouch, R. J.; Yang, W. *EMBO J.* **2008**, *27*, 1172.
(53) Nowotny, M.; Gaidamakov, S. A.; Ghirlando, R.; Cerritelli, S. M.; Crouch, R. J.; Yang, W. *Mol. Cell* **2007**, *28*, 264.
(54) Nowotny, M.; Yang, W. *EMBO J.* **2006**, *25*, 1924.
(55) Ho, M.-H.; De Vivo, M.; Dal Peraro, M.; Klein, M. L. *J. Am. Chem. Soc.* **2010**, *132*, 13702.
(56) De Vivo, M.; Dal Peraro, M.; Klein, M. L. *J. Am. Chem. Soc.* **2008**, *130*, 10955.
(57) Rosta, E.; Woodcock, H. L.; Brooks, B. R.; Hummer, G. *J. Comput. Chem.* **2009**, *30*, 1634.
(58) Elsasser, B.; Fels, G. *Phys. Chem. Chem. Phys.* **2010**, *12*, 11081.
(59) Aaqvist, J.; Warshel, A. *J. Am. Chem. Soc.* **1990**, *112*, 2860.
(60) Chaudret, R.; Piquemal, J.-P.; Cisneros, G. A. *Phys. Chem. Chem. Phys.* **2011**, *13*, 11239.
(61) Solt, I.; Simon, I.; Csaszar, A. G.; Fuxreiter, M. *J. Phys. Chem. B* **2007**, *111*, 6272.
(62) Coleman, J. E.; Nakamura, K.; Chlebowski, J. F. *J. Biol. Chem.* **1983**, *258*, 386.
(63) Koutsioulis, D.; Lyskowski, A.; Mäki, S.; Guthrie, E.; Feller, G.; Bouriotis, V.; Heikinheimo, P. *Protein Sci.* **2010**, *19*, 75.
(64) Garcin, E. D.; Hosfield, D. J.; Desai, S. A.; Haas, B. J.; Bjoras, M.; Cunningham, R. P.; Tainer, J. A. *Nat. Struct. Mol. Biol.* **2008**, *15*, 515.
(65) Nakamura, T.; Zhao, Y.; Yamagata, Y.; Hua, Y.-j.; Yang, W. *Nature* **2012**, *487*, 196.
(66) Ivanov, I.; Tainer, J. A.; McCammon, J. A. *Proc. Natl. Acad. Sci. U.S.A.* **2007**, *104*, 1465.
(67) Hosfield, D. J.; Guan, Y.; Haas, B. J.; Cunningham, R. P.; Tainer, J. A. *Cell* **1999**, *98*, 397.
(68) Lans, I.; Medina, M.; Rosta, E.; Hummer, G.; Garcia-Viloca, M.; Lluch, J. M.; González-Lafont, À. *J. Am. Chem. Soc.* **2012**, *134*, 20544.
(69) E, W.; Ren, W.; Vanden-Eijnden, E. *J. Phys. Chem. B* **2005**, *109*, 6688.
(70) Shao, Y.; et al. *Phys. Chem. Chem. Phys.* **2006**, *8*, 3172.
(71) Becke, A. D. *J. Chem. Phys.* **1993**, *98*, 5648.
(72) Brooks, B. R.; Bruccoleri, R. E.; Olafson, B. D.; States, D. J.; Swaminathan, S.; Karplus, M. *J. Comput. Chem.* **1983**, *4*, 187.
(73) Brooks, B. R.; et al. *J. Comput. Chem.* **2009**, *30*, 1545.
(74) Woodcock, H. L.; Hodoscek, M.; Gilbert, A. T. B.; Gill, P. M. W.; Schaefer, H. F., III; Brooks, B. R. *J. Comput. Chem.* **2007**, *28*, 1485.
(75) Fukunishi, H.; Watanabe, O.; Takada, S. *J. Chem. Phys.* **2002**, *116*, 9058.
(76) Kumar, S.; Rosenberg, J. M.; Bouzida, D.; Swendsen, R. H.; Kollman, P. A. *J. Comput. Chem.* **1992**, *13*, 1011.
(77) Truhlar, D. G.; Garrett, B. C. *Acc. Chem. Res.* **1980**, *13*, 440.
(78) Pavlov, M.; Siegbahn, P. E. M.; Sandstrom, M. *J. Phys. Chem. A* **1998**, *102*, 219.
(79) Baldwin, G. S.; Sessions, R. B.; Erskine, S. G.; Halford, S. E. *J. Mol. Biol.* **1999**, *288*, 87.
(80) Dudev, T.; Lim, C. *Annu. Rev. Biophys* **2008**, *37*, 97.
(81) Yatsimirskii, K. B.; Vasilév, V. P. *Instability Constants of Complex Compounds*; Pergamon Press: Elmsford, NY, 1960.
(82) Nowotny, M. *EMBO Rep.* **2009**, *10*, 144.
(83) Yang, W.; Steitz, T. A. *Structure* **1995**, *3*, 131.
(84) Uchiyama, Y.; Miura, Y.; Inoue, H.; Ohtsuka, E.; Ueno, Y.; Ikehara, M.; Iwai, S. *J. Mol. Biol.* **1994**, *243*, 782.
(85) Reiter, N. J.; Osterman, A.; Torres-Larios, A.; Swinger, K. K.; Pan, T.; Mondragon, A. *Nature* **2010**, *468*, 784.
(86) Mondragón, A. *Ann. Rev. Biophys.* **2013**, *42*, 537.
(87) Smith, D.; Pace, N. R. *Biochemistry* **1993**, *32*, 5273.
(88) Grosshans, C. A.; Cech, T. R. *Biochemistry* **1989**, *28*, 6888.
(89) McConnell, T. S.; Herschlag, D.; Cech, T. R. *Biochemistry* **1997**, *36*, 8293.
(90) Marcia, M.; Pyle, A. M. *Cell* **2012**, *151*, 497.
(91) Lehman, N.; Joyce, G. F. *Nature* **1993**, *361*, 182.
(92) Keck, J. L.; Goedken, E. R.; Marqusee, S. *J. Biol. Chem.* **1998**, *273*, 34128.
(93) Weston, J. *Chem. Rev.* **2005**, *105*, 2151.